Theoretical and numerical investigation of bending properties of Cu nanowires

H.F. Zhan and Y.T. Gu*

School of Engineering Systems, Queensland University of Technology, Brisbane, 4001, Australia

***Corresponding author:** Dr. Yuantong Gu

Mailing Address: School of Engineering Systems,

Queensland University of Technology,

GPO Box 2434, Brisbane, QLD 4001, Australia

Telephones: +61-7-31381009

Fax: +61-7-31381469

E-mail: yuantong.gu@qut.edu.au

Abstract: Based on the AFM-bending experiments, a molecular dynamics (MD) bending simulation model is established which could accurately account for the full spectrum of the mechanical properties of NWs in a double clamped beam configuration, ranging from elasticity to plasticity and failure. It is found that, loading rate exerts significant influence to the mechanical behaviours of nanowires (NWs). Specifically, a loading rate lower than 10 *m/s* is found reasonable for a homogonous bending deformation. Both loading rate and potential between the tip and the NW are found to play an important role in the adhesive phenomenon. The force versus displacement (*F-d*) curve from MD simulation is highly consistent in shapes with that from experiments. Symmetrical *F-d* curves during loading and unloading processes are observed, which reveal the linear-elastic and non-elastic bending deformation of NWs. The typical bending induced tensile-compressive features are observed. Meanwhile, the simulation results are excellently fitted by the classical Euler-Bernoulli beam theory with axial effect. It is concluded that, axial tensile force becomes crucial in bending deformation when the beam size is down to nanoscale for double clamped NWs. In addition, we find shorter NWs will have an earlier yielding and a larger yielding force. Mechanical properties (Young's modulus & yield strength) obtained from both bending and tensile deformations are found comparable with each other. Specifically, the modulus is essentially similar under these two loading methods, while the yield strength during bending is observed larger than that during tension.

Keywords: Bending, Nanowires, Mechanical Properties, Beam Theory, Molecular Dynamics Simulation

1. Introduction

NWs are attracting increasing applications in diverse areas, such as the nanocomposites strengtheners [1], the active components of nanoelectromechanical systems (NEMS) including high frequency resonator [2, 3], force and pressure sensing [4], ultrahigh-resolution mass sensing [5], and other devices [6, 7]. Therefore, understanding of the mechanical properties of nanowires (NWs) is extremely important from both scientific and technological viewpoints. To probe into the NWs mechanical properties, researchers have carried out various experimental studies. For instance., based on the scanning tunnel microscope (STM) and scanning electron microscope (SEM), Dikin et al. [8] studied the resonance vibration of amorphous SiO_2 NWs. A number of atomic force microscope (AFM)-based compression, bending and nanoindentation studies of NWs have also been conducted [9-12]. According to the in *situ* tensile tests, Richter et al. [13] confirmed that the properties of nanomaterials can be engineered by controlling defect and flaw densities. Seo et al. [14] found the defect-free Au NWs appear superplasticity on tensile deformation. Recently, Yue et al. [15] reported the ultrahigh elastic strains that can be sustained in Cu NWs using in situ tensile experiments. It is certain that, experimental studies could provide affluent and meaningful information on the

mechanical properties of NWs. However, due to the extremely small dimensions of NWs, the manipulation of these experiments is involving with huge challenges (e.g., the precise control of the pinning points of the NW), and the measurements of certain properties are also suffering from complications due to wire-substrate friction [16].

In view of the deficiency of experiments, various numerical approaches are then proposed by researchers, such as *ab initio* calculation, multi-scale simulation and MD simulation [17]. Especially, the MD simulation is the most frequently applied method. In recent years, tremendous MD studies have been reported investigating the mechanical properties or deformation behaviours of NWs under diverse loading conditions. For example, the investigation of NWs mechanical properties under tensile deformation, including the influence from factors of strain rate, temperature, surface defects and others [18-21]. Other NWs deformations such as compression (buckling) and torsion have also been widely investigated [22-24]. Researchers found that, due to the significant surface-to-volume ratio of NW, a plethora of novel mechanical behaviours are emerged, such as the phase transformations [25], pseudoelastic behaviour [26] and shape memory [27, 28] effect. Particularly, majority of current MD simulations have focused on the mechanical analysis of NWs subjected to uniaxial load. Therefore, it is of great importance to exploit the mechanical behaviour of NWs under bending deformation.

Although atomistic studies of the NWs bending behaviour have been pursued, these investigations usually focused on dynamic deformation behaviour instead of mechanical properties [29, 30]. For instance, Zheng et al. [31] reported the formation of two conjoint fivefold deformation twins (DFTs) in Cu NWs under bending. Some works did investigate the Young's modulus of NWs under bending, however, a complete description of the bending deformation including the elastic and plastic deformation as well as failure is still lack, e.g., the work by McDowell et al. [32], and Chan et al. [33]. Furthermore, previous bending studies usually considered a displacement or force load directly applied to the NW instead using a real tip. For example, Wu [34] investigated the bending response of a Cu cantilever NW by applying a lateral force at one end of NW.

Therefore, in this work, we propose a three-point bending model by MD simulations for double clamped NWs. This bending model is established according to the AFM-bending method proposed by Wu et al. [16, 35], who suggested that such bending approach could provide unambiguous measurements of the full spectrum of NWs mechanical properties, including Young's modulus *E*, yield strength, plastic deformation and failure. To best mimic the real AFM-based bending experimental conditions, a real rigid tip is implemented during MD simulation. Note that, similar simulation model is initially discussed by Yan et al. [36], however, according to our simulation results, the loading rate applied by them seems to be too large, which might lead to inaccuracy on reflecting the actual deformation properties of Cu NW under bending. Therefore, we present a complete discussion of this three-point bending model in this work. Different factors including loading rate, as

well as adhesion effect is investigated. Furthermore, the classical Euler-Bernoulli beam theory with and without axial effect are discussed and compared with the MD results.

2. Numerical Implementation

2.1 Molecular Dynamics Setting

Molecular dynamics (MD) simulations are carried out on double clamped Cu NWs subjected to pure bending deformation. The Large-scale Atomic/Molecular Massively Parallel simulator (LAMMPS) [37] is employed to carry out the MD simulation. Square cross-section Cu NW with the initial atomic configuration positioned at perfect FCC lattice site is considered, and the *x*, *y* and *z* coordinate axes represent the lattice direction of [100], [010], [001], respectively. The simulation model is shown in Fig. 1. In detail, the NW is divided into two regions, including boundary region and mobile region. To mimic the clamped boundary condition, boundary regions in two ends are fixed in all three dimensions (*x*, *y* and *z*). A rigid diamond cylinder tip is employed to impose the bending load. As illustrated in Fig. 1, the initial distance between the tip and NW is 0.3615 *nm*, and the tip has a radius of 1.0845 *nm* and a length of 5.784 *nm*. The size of the NW is denoted as $h \times h \times L$. No periodic boundary condition is adopted.

The following embedded-atom-method (EAM) potential [38, 39] as developed by Mishin [40] is used to describe the Cu-Cu atomic interactions in these simulations.

$$E_{tot} = \sum_i F(\rho_i) + \frac{1}{2}\sum_i \sum_j V(r_{ij}) \ , \rho_i = \sum_j \Phi(r_{ij}) \tag{1}$$

here V, F, ρ are the pair potential, the embedded energy, and the electron cloud density, respectively. *i* and *j* are the number of atoms, and r_{ij} is the distance between them. This potential is chosen as it can reliably predict the material stacking faults energies and the stability of nonequilibrium structures of copper. For the Cu-C interaction, Morse potential is adopted, which is expressed by:

$$U(r) = D[e^{-2a(r-r_0)} - 2e^{a(r-r_0)}] \tag{2}$$

where *r* is the length of a Cu-C bond and *D*, *a*, and r_0 correspond to the cohesive energy, the elastic modulus, and the atomistic distance at equilibrium, respectively. Two sets of *D*, *a* and r_0 applied by Hsieh et al. [41] and Yan et al. [42] are adopted, which are referred as M1 and M2 respectively as listed in Table 1. Note that, M2 is only applied when discussing the adhesive phenomenon due to the potential effect. The equations of motion are integrated with time using a Velocity Verlet algorithm [43].

During each simulation, NWs are first relaxed to a minimum energy state using the conjugate gradient energy minimization and then the Nose-Hoover thermostat [44, 45] is employed to equilibrate the nanowires at 0.01 *K*. After that, a constant velocity is imposed to the tip. In order to analyse the partial

dislocation and stacking faults (SFs) during the tensile deformation, the centro-symmetry parameter [46] (*csp*) is used, which is defined by

$$csp = \sum_{i=1,6} \left| \vec{R}_i + \vec{R}_{i+6} \right|^2 \tag{3}$$

where $\vec{R}_i$ and $\vec{R}_{i+6}$ are vectors corresponding to the six pairs of opposite nearest neighbours in FCC lattice. The *csp* value increases from 0 for perfect FCC lattice to positive values for defects and for atoms close to free surfaces. In this work, $0.5 < csp \le 3$, $3 < csp \le 12$, and $csp > 12$ are assigned to identify the partial dislocations, stacking faults (SFs) and surface atoms, respectively.

In addition, the virial atomic stress tensor is also adopted to reveal the bending deformation of NWs, which is defined as:

$$S_{\alpha\beta} = -\sum_i m_i v_i^\alpha v_i^\beta + \frac{1}{2}\sum_i \sum_{j \ne i} F_{ij}^\alpha F_{ij}^\beta \tag{4}$$

where m_i and v_i are the mass and velocity of the atom *i*, F_{ij} is the force between atom *i* and *j*, r_{ij} is the distance between atoms *i* and *j*, and the indices α and β denote the Cartesian components.

3. Parametric Study

For validation, MD results are first compared with experimental measurements. Fig. 2 represents the force versus displacement (*F-d*) curve of Cu NWs during loading and unloading processes. Consistent in shapes with the experimental results of Au NWs reported by Wu et al. [16], we observe a nearly symmetric *F-d* curve. Such consistency suggests that the MD model could provide validate information about the bending deformation properties of NWs. Further investigations of the simulation model are then discussed as below. Note that, a relative short Cu NW with the size of $2.892 \times 2.892 \times 14.46$ nm^3 is chosen in this section to save the computational cost.

3.1 Loading Rate Effect

It is generally accepted that, loading rates could exert great influence to the performance of NWs. Therefore, it is crucial to examine the possible loading rate effect, as well as the reasonable loading rate for a bending deformation. In this section, several different loading rates including 50 *m/s*, 15 *m/s*, 10 *m/s*, 6 *m/s*, 4 *m/s*, 2 *m/s*, and 1 *m/s* have been considered.

Fig. 3 shows the *F-d* curves under different loading rates. As the reaction force resulted from the high loading rate of 50 *m/s* is very large (around 230 *nN* at the maximum displacement), thus, its *F-d* curve is excluded from Fig. 3. To note that, each *F-d* curve is obtained from a circle loading process, i.e., the NW is first loaded to the deflection of 1.2 *nm* and then unloaded to the initial state under the same constant loading rate. It is evident from Fig. 3(a) that, higher loading rate is always corresponding with larger reaction force. Such observation is consistent with the finding for NWs under tensile

deformation [47], i.e., higher loading rate induces larger yielding strength. As illustrated in Fig. 3(a), a reaction force around 58 *nN* is found for the loading rate of 15 *m/s* at the displacement of 1.2 *nm*, while, for the loading rate of 1 *m/s*, the reaction force is found only around 20 *nN*. Particularly, the reaction force is found to fluctuate with smaller amplitude for lower loading rate. As seen in Fig. 3(b) and 3(c), this trend is much more obvious at the beginning of loading, as well as at the maximum displacement.

It is found that, loading rate smaller than 10 m/s is tend to produce similar *F-d* curve during loading and unloading, e.g., the loading rate of 2 *m/s* and 1 *m/s*. However, for large loading rate (such as 50 *m/s*), the *F-d* curves during loading and unloading are totally different. According to the experimental results by Wu et al. [16], the asymmetry *F-d* curve during the whole loading circle is actually indicating plastic deformation happened during loading. To investigate this issue, several atomic configurations of the NW are presented in Fig. 4.

In general, loading rate is found to exert large influence to the deformation behaviours of NWs. As illustrated in Fig. 4(a2), the high loading rate of 50 *m/s* behaviours like an impact load, leading a severe local plastic deformation underneath the tip. The NW structure beneath the tip is found in an amorphous state, with the rest appears unchanged. For the loading rate of 15 *m/s*, an intrinsic stacking fault (SF) is generated under the tip at the displacement of 1.05 *nm*, indicating the local plastic deformation emerged. Comparing with these two cases, loading rate of 1 *m/s* shows a homogenous bending deformation at the displacement of 1.05 *nm*. According to Fig. 4(c1), no obvious stress concentration is observed beneath the tip, and the entire NW is still in perfect FCC structure as revealed in Fig. 4(c2). It should be noted that, although the loading rate of 1 *m/s* is eight orders larger than the typical experimental value of 50 *nm/s* [16], it is already a very slow loading rate in the atomistic system, which could be taken as quasistatic. In all, we could conclude that, when the loading rate is fairly slow, the loading rate effect would be ignorable, and to perform a homogenous bending deformation, the loading rate should be below 10 *m/s*. In the meanwhile, high loading rate would induce large reaction force, and cause plastic deformation underneath the tip. Based on these conclusions, we find the loading rate of 200 *m/s* adopted by Yan et al. [36] seems too large for a Cu NW bending simulation, which might lead to inaccuracy on reflecting the actual deformation properties of Cu NWs.

3.2 Adhesive Phenomenon

Another issue arisen from the *F-d* curve in Fig. 3(a) is the negative value of the reaction force, which is indeed the adhesive force between the tip and NW. As primarily discussed by Yan et al. [36], the thinner of the NW, the larger the NW deforms due to the adhesive force. Besides of this size effect, our simulations suggest other factors also exert obvious influence to the adhesive phenomenon, e.g., loading rate and atomic interaction between the tip and NW. As previously presented in Fig. 3(b),

almost a same maximum adhesive force (around 2.0 *nN*) is observed for all loading rates at the beginning of loading. However, this is not the case during unloading process. From Fig. 5(a), we find for loading rate lower than 10 *m/s*, the adhesive force is uniformly around 4.5 *nN*. But for high loading rate, the adhesive force and the corresponding displacement appears very different. We find that, the higher the loading rate is, the smaller adhesive force appears. Atomic configurations in Fig. 4 provide a good explanation for the diverse adhesive phenomenon. For high loading rate, the full recovery of the plastic deformation during unloading is not possible. The recovery speed is smaller than the unloading rates, which finally induces early separation between the tip and NW. It is noteworthy that, the plastic deformation for the NW under the loading rate of 15 m/s is still small, which is also fully recovered as shown in Fig. 4(b3).

Two kinds of Cu-C Morse potential parameters (M1 and M2 as listed in Table 1) are employed to examine the potential effect to the adhesive phenomenon. To make comparison, a same size rigid virtual cylinder tip is also adopted. The virtual tip is similar as the spherical indenter tip applied by previous researchers during nanoindentation with no real shape [47, 48]. In particular, the virtual tip will exert a repulsive force between the tip and the NW, which is expressed as $F(r) = -k(r-R)^2$, here k is the specified force constant, r is the distance from the atom to the centre of the tip and R is radius of the tip. Fig. 5(b) shows the *F-d* curves during loading for these three different interactions between the tip and NW. As the virtual tip only provides repulsive force between the tip and NW, thus, no adhesive force is revealed in the *F-d* curve. According to Fig. 5(b), different adhesive force is produced from these sets of Morse potential parameters. In particular, the adhesive force is about 2.0 *nN* and 7.5 *nN* for the Morse potential of M1 and M2, respectively. It is interesting to mention that, although the adhesive phenomenon diverges with different potential, the entire *F-d* curve is almost parallel to each other. Such finding indicates different potentials exhibit little influence to the whole deformation behaviours of NWs. Conclusively, both loading rate and potential play an important role in the adhesive phenomenon.

4. Theoretical and Numerical Analysis for Bending Properties of Cu NWs

4.1 Theoretical Analysis

According to classical Euler-Bernoulli beam theory (EBT), Young's modulus is related by the beam displacement d and the applied load F. For the double clamped beam discussed here, the resulting *F-d* curve is described by the following well-known equation [49]:

$$F = \frac{192EI}{L^3} d \tag{5}$$

where F is the load applied to the centre of the beam, d is the resulting displacement of the beam at the load position, E is the Young's modulus of the beam, I is the moment of inertia, and L is the beam

length. For square cross-section NW applied here, $I = h^4/12$ (h is the NW's cross-sectional size). Apparently, for a given NW, Eq. 5 has predicted a linear relationship between F and d.

Generally, when the beam is displaced, an axial tensile force is inherently induced due to the stretching of the beam. The common practice in continuum mechanics is to disregard this stretching force as it has no noticeable effect on the behaviour of the beam [49]. However, when the size is down to nano-scale, such stretching force is expected to exert obvious influence to the beam bending behaviours, particularly when the NW is double clamped. By incorporating the contribution of the stretching force to the governing beam equation [50], Heidelberg et al. [51] proposed a modified nonlinear relationship between F and d:

$$F = \frac{192EI}{L^3} f(k)d\,,\quad f(k) = \frac{k}{48 - 192\tanh(\sqrt{k}/4)/\sqrt{k}} \tag{6}$$

where k is solved from a complex transcendental equation, with the asymptotic solution given as:

$$k = \frac{6s(140+s)}{350+3s}\,,\quad s = d^2\frac{A}{I} \tag{7}$$

Here, A is the cross-sectional area. The yield strength is then estimated from the yield force F_y in F-d curve before the onset of plastic deformation according to [49]:

$$\sigma_y = \frac{3F_yL}{4h^3} \tag{8}$$

4.2 Bending Properties of NWs

Based on the parametric study in Section 3, an in-detail discussion of the bending deformation of Cu NW is then carried out. The loading rate of 1 *m/s* is applied in this section. Basically, in subsection 4.2.1, a complete investigation of the bending deformation is conducted, with the adopted NW size as $2.892 \times 2.892 \times 32.535$ nm^3. In subsection 4.2.2, the mechanical properties (Young's modulus & yield strength) obtained from a group of Cu NWs under bending and tensile deformations are compared. These Cu NWs have the same cross-sectional size as $2.892 \times 2.892\,nm^2$, but different lengths ranging from 14.46 *nm* to 32.535 *nm*.

4.2.1 Comparison of Theoretical and Numerical Studies

Fig. 6(a) ~ (c) presents the F-d curves obtained during three cycles of repeated loading and unloading processes. In Fig. 6(a), the slope of the F-d curve during loading and unloading is found identical, and the F-d curve in both Fig. 6(a) and (b) appears symmetrical along the dashed line. According to Heidelberg et al. [51], these symmetrical F-d curves indicates the linear-elastic or non-elastic bending deformation of NWs, respectively. In other words, the NW is elastically loaded and unloaded. The subsequent atomic configurations in Fig. 7(a) ~ (c) reveal that no plastic deformation happens to the NW at the displacement of 2.9 *nm*, and the NW recovers to the original state after full unloaded.

However, increased loading eventually results in plastic deformation. From Fig. 6(c) and (d), a clear break is followed with the same initial elastic deformation region in Fig. 6(b), which corresponds to the yield point. According to Fig. 6(d), we find the reaction force is fluctuating around 15 *nN* after yielding, which implies the deformation occurs more readily afterwards. As illustrated in Fig. 7(d), partial dislocations are already nucleated beneath the tip at the displacement of 4.5 *nm* with the NW being obviously elongated, indicating the emergence of plastic deformation. Further loading eventually resulted in the failure of the NW, as shown in Fig. 7(e).

The typical bending induced tensile-compressive features as mentioned by Yan et al. [36] are also observed. As seen in Fig. 6(b), three regions are found under the largest strain state, i.e., regions A1 and A3 near the end, and regions A2 beneath the tip. Particularly, in region A2, the upper surface is observed under compressive state, with the bottom surface under tensile state. Furthermore, we find the partial dislocations are first nucleated around these regions, indicating they are preferred to deform plastically. From Fig. 7(e), these three regions are found to be occupied by partial dislocations when the NW is almost failure. In conclusion, consistent with the experimental results [35], this model allows the full spectrum of mechanical properties to be measured, ranging from elasticity to plasticity and failure.

To calculate the related mechanical properties including Young's modulus and yield strength, further discussions on the *F-d* curve in Fig. 6(d) are needed. Similar as discussed by Heidelberg et al. [51], the *F-d* curve is found linear-elastic when the displacement is smaller than half of one cross-sectional size, i.e., $d<0.5h$, which could be accurately predicted by the classical theory of Eq. 5. However, nonlinear pattern of *F-d* curve is generated as the displacement approaches one cross-section size. As pointed out in Fig. 6(d), the *F-d* curve becomes increasingly nonlinear as the displacement *d* passes *h*, and eventually leading to an ultimate cubic-like dependence on the displacement. It is obvious that Eq. 5 is no longer applicable to such nonlinear *F-d* curve, and the nonlinear Eq. 6 should be considered. In order to test the accuracy of Eq. 6, we follow the same fitting procedure applied by previous researchers [35], i.e., using the data at small displacement to fit, and then extend to include increasingly larger displacement. Specifically, in this work, MD data that fall in the displacement between 0 and $0.5h$, 0 and h are employed to fit with Eq. 5 and 6, respectively.

The fitting results by Eq. 5 and 6 are compared in Fig. 6(d). Just as expected, we find the classic theory (Eq. 4) only matches the simulation results when the displacement is smaller than $0.5h$. It can be concluded that without considering axial tensile force, Eq. 4 provides very poor description of the mechanical properties of NWs when the displacement is fairly large. In the contrast, the prediction results by Eq. 6 at larger displacement ($d>h$) are excellently agreed with the MD results until the NW reaches yield point. The excellent fit not only demonstrates that Eq. 5 is very good in interpreting the bending deformation of double clamped NWs with large deflection, but also suggests that the axial tensile force becomes crucial in bending deformation when the beam size is down to nanoscale.

Therefore, Eq. 5 that proposed based on the experimental measurements is found also suitable with the MD results.

4.2.2 Young's Modulus and Yield Strength

Based on the above simulation model, further investigations of NW mechanical properties are then conducted. The *F-d* curves obtained from a group of Cu NWs are compared in Fig. 8(a). It is apparent that short NWs reveal early yielding, and also a large yielding force. In the meanwhile, a linear-elastic *F-d* curve is usually formed for short NWs, with nonlinear-elastic *F-d* curve generated for long NWs. The nonlinearity increases with the increasing of NW's length. To compare the mechanical properties with tensile deformation, we also consider the NWs in this group under tensile loading. Comparisons are discussed as below.

Fig. 8(b) plots the estimated Young's modulus *E* by Eq. 5 and 6, together with the values from tensile deformation, which are determined directly from the stress-strain curves with the strain <3%. Evidently, the modulus values obtained from tensile deformation and Eq. 5 are very close to each other. However, certain disparity in modulus values appears as the NW length decreases. One possibility reason for such disparity is supposed due to the clamped condition in NW's two ends. As seen in Fig. 8(b), the modulus values become more stable when the NW is longer than 20 *nm*, suggesting the boundary conditions of NWs affect a shorter NW more significantly than a longer NW. The similarity of Young's modulus between tension and bending is actually showing certain discrepancy with previous works [32, 52]. Several factors are assumed contributing to such discrepancy, including the size of NWs, NW's orientation, NW's ending conditions, and the calculation techniques of modulus. Our estimations of *E* are also in good agreement with previous studies. For instance, a value of 70 *GPa* was reported for Cu NW under tensile deformation by Liang and Zhou [53]. Accordingly, we find modulus values from Eq. 6 appear smaller than those from Eq. 5. This finding is reasonable, as the stretching force leads to an enhancement of its rigidity [50]. Therefore, employing Eq. 6 to fit with the MD results, a smaller Young's modulus would be obtained.

The yield strength during bending deformation is also calculated according to Eq. 8 before the onset of plastic deformation. Comparisons are made with the yield strength during tensile deformation in Fig. 8(c). It is found that the yield strength during bending is larger than that during tensile deformation. Particularly, the yield strength from bending results increases with the increasing of NW length, while for tensile deformation, the yield strength appears almost the same (around 8 *GPa*). We expect that the bending deformation of the double clamped NW is always accompanied with the inherently induced tension, which thus, resulted in different yield strength. Furthermore, the increasing trend of yield strength is indeed indicating the increasing influence of axial tensile force as the NW length increases.

In general, the simulation model as well as the modified beam theory with axial effect provides a effective way to study the mechanical properties of NWs. Young's modulus and yield strength obtained from both bending deformation and tensile deformation are comparable with each other. However, as seen in Fig. 8(b), disparities are observed in the values of Young's modulus when the NW length is small. Previous researchers have proposed different explanations for this size dependence property, e.g., Miller and Shenoy [54] suggest that the changes in elastic modulus are primarily because of the surface elasticity. Other factors are also observed to result the observed trends in modulus, such as the nonlinear elastic response of the NW core when NWs subjected to uniaxial loads [55]. Therefore, further studies are required to identify the size dependence property of Young's modulus.

4. Conclusion

Conclusively, based on the AFM-bending experiments, we have established a MD bending simulation model which could accurately account for the mechanical properties of NWs in a clamped-clamped beam configuration. The classical Euler-Bernoulli beam theory with and without considering axial effect are discussed and compared with the MD results. The Young's modulus and yield strength estimated from bending deformation are compared with those from tensile deformation. Major conclusions are summarised as below:

1) Loading rate exerts significant influence to the mechanical behaviours of NWs. High loading rate would induce severe local plastic deformation beneath the tip, or even leading the deformed area in an amorphous state. The higher loading rate usually induces higher reaction force. A loading rate lower than 10 *m/s* is found reasonable for a homogonous bending deformation;
2) Both loading rate and potential between the tip and the NW are found to play an important role in the adhesive phenomenon. In particular, different potential parameters show obvious influence to the adhesive force, but exhibit little influence to the whole deformation behaviours of NWs;
3) The AFM-bending procedures are reproduced by the MD simulation. The force versus displacement (*F-d*) curve is highly consistent in shapes with those obtained from experiments. Symmetrical *F-d* curves during loading and unloading processes are observed, which reveal the linear-elastic and non-elastic bending deformation of NWs;
4) Full spectrum of mechanical properties of NWs, ranging from elasticity to plasticity and failure are unambiguously revealed by the MD simulation. In addition, the typical bending induced tensile-compressive features is observed;
5) Consistent with the experimental results, the *F-d* curve is linear-elastic when the displacement is smaller than half of one cross-sectional size, i.e., $d<0.5h$. When the displacement increases, nonlinear pattern of *F-d* curve is shown, with the nonlinearity increases as the displacement pass one cross-sectional size;

6) The simulation results are excellently fitted by the classical Euler-Bernoulli beam theory with the consideration of axial effect. It is concluded that, axial tensile force becomes crucial in bending deformation when the beam size is down to nanoscale for double clamped NWs, especially when the deflection is fairly large;
7) For short NWs, an early yielding and a large yielding force are observed. In the meanwhile, a linear-elastic *F-d* curve is usually formed for short NWs, with nonlinear-elastic *F-d* curve generated for long NWs. The nonlinearity increases with the increasing of NW's length;
8) Mechanical properties (Young's modulus & yield strength) obtained from both bending and tensile deformations are comparable with each other. Specifically, the modulus is essentially similar under these two loading methods, while the yield strength during bending is observed larger than that during tension.

References:

[1] M. Kawamura, N. Paul, V. Cherepanov, B. Voigtländer, Phys. Rev. Lett., 91 (2003) 96102.
[2] A. Husain, J. Hone, H.W.C. Postma, X. Huang, T. Drake, M. Barbic, A. Scherer, M. Roukes, Appl. Phys. Lett., 83 (2003) 1240.
[3] M. Li, T.S. Mayer, J.A. Sioss, C.D. Keating, R.B. Bhiladvala, Nano Lett., 7 (2007) 3281-3284.
[4] D. Rugar, R. Budakian, H. Mamin, B. Chui, Nature, 430 (2004) 329-332.
[5] Y. Yang, C. Callegari, X. Feng, K. Ekinci, M. Roukes, Nano Lett., 6 (2006) 583-586.
[6] N. Hu, Y. Karube, C. Yan, Z. Masuda, H. Fukunaga, Acta Mater., 56 (2008) 2929-2936.
[7] K. Eom, H.S. Park, D.S. Yoon, T. Kwon, Phys. Rep., (2011).
[8] D. Dikin, X. Chen, W. Ding, G. Wagner, R. Ruoff, J. Appl. Phys., 93 (2003) 226.
[9] M. Riaz, O. Nur, M. Willander, P. Klason, Appl. Phys. Lett., 92 (2008) 103118.
[10] J. Song, X. Wang, E. Riedo, Z.L. Wang, Nano Lett., 5 (2005) 1954-1958.
[11] S. Hoffmann, I. Utke, B. Moser, J. Michler, S.H. Christiansen, V. Schmidt, S. Senz, P. Werner, U. Gösele, C. Ballif, Nano Lett., 6 (2006) 622-625.
[12] L.W. Ji, S.J. Young, T.H. Fang, C.H. Liu, Appl. Phys. Lett., 90 (2007) 033109-033109-033103.
[13] G. Richter, K. Hillerich, D.S. Gianola, R. Mo nig, O. Kraft, C.A. Volkert, Nano Lett., 9 (2009) 3048-3052.
[14] J.H. Seo, Y. Yoo, N.Y. Park, S.W. Yoon, H. Lee, S. Han, S.W. Lee, T.Y. Seong, S.C. Lee, K.B. Lee, Nano Lett., (2011).
[15] Y. Yue, P. Liu, Z. Zhang, X.D. Han, E. Ma, Nano Lett., (2011).
[16] B. Wu, A. Heidelberg, J.J. Boland, Nat. Mater., 4 (2005) 525-529.
[17] S. Liu, N. Hu, G. Yamamoto, Y. Cai, Y. Zhang, Y. Liu, Y. Li, T. Hashida, H. Fukunaga, Carbon, (2011).
[18] H.S. Park, J.A. Zimmerman, Phys. Rev. B, 72 (2005) 54106.
[19] K. Gall, J. Diao, M.L. Dunn, Nano Lett., 4 (2004) 2431-2436.
[20] J. Diao, K. Gall, M.L. Dunn, J. Mech. Phys. Solids, 52 (2004) 1935-1962.
[21] H.F. Zhan, Y.T. Gu, C. Yan, X.Q. Feng, P. Yarlagadda, Comput. Mater. Sci., 50 (2011) 3425-3430.
[22] P.A.T. Olsson, H.S. Park, Acta Mater., 59 (2011) 3883–3894.
[23] S. Jiang, H. Zhang, Y. Zheng, Z. Chen, J. Phys. D: Appl. Phys., 42 (2009) 135408.
[24] H.F. Zhan, Y.T. Gu, C. Yan, P.K.D.V. Yarlagadda, Advanced Materials Research, 335 (2011) 498-501.
[25] J. Diao, K. Gall, M.L. Dunn, Nat. Mater., 2 (2003) 656-660.
[26] H.S. Park, K. Gall, J.A. Zimmerman, Phys. Rev. Lett., 95 (2005) 255504.
[27] W. Liang, M. Zhou, F. Ke, Nano Lett., 5 (2005) 2039-2043.
[28] H.S. Park, C. Ji, Acta Mater., 54 (2006) 2645-2654.
[29] M. Menon, D. Srivastava, I. Ponomareva, L.A. Chernozatonskii, Phys. Rev. B, 70 (2004) 125313.
[30] G. Yun, H. Park, Phys. Rev. B, 79 (2009) 195421.
[31] Y. Zheng, H. Zhang, Z. Chen, L. Wang, Z. Zhang, J. Wang, Appl. Phys. Lett., 92 (2008) 041913.
[32] M. McDowell, A. Leach, K. Gall, Modell. Simul. Mater. Sci. Eng., 16 (2008) 045003.
[33] W.K. Chan, M. Luo, T.Y. Zhang, Scripta Mater., 59 (2008) 692-695.
[34] H. Wu, Comput. Mater. Sci., 31 (2004) 287-291.
[35] B. Wu, A. Heidelberg, J.J. Boland, J.E. Sader, X.M. Sun, Y.D. Li, Nano Lett., 6 (2006) 468-472.

[36] Y. Yan, J. Zhang, T. Sun, W. Fei, Y. Liang, S. Dong, Appl. Phys. Lett., 93 (2008) 241901.
[37] S. Plimpton, P. Crozier, A. Thompson, in, Sandia National Lab, 2007.
[38] S. Foiles, M. Baskes, M. Daw, Phys. Rev. B, 33 (1986) 7983-7991.
[39] M. Daw, M. Baskes, Phys. Rev. B, 29 (1984) 6443-6453.
[40] Y. Mishin, M. Mehl, D. Papaconstantopoulos, A. Voter, J. Kress, Phys. Rev. B, 63 (2001) 224106.
[41] J. Hsieh, S. Ju, S. Li, C. Hwang, Phys. Rev. B, 70 (2004) 195424.
[42] Y. Yan, T. Sun, S. Dong, X. Luo, Y. Liang, Appl. Surf. Sci., 252 (2006) 7523-7531.
[43] S. Plimpton, J. Comput. Phys., 117 (1995) 1-19.
[44] W.G. Hoover, Phys. Rev. A, 31 (1985) 1695-1697.
[45] S. Nosé, J. Chem. Phys., 81 (1984) 511.
[46] C. Kelchner, S. Plimpton, J. Hamilton, Phys. Rev. B, 58 (1998) 11085-11088.
[47] H.F. Zhan, Y.T. Gu, P. Yarlagadda, Adv. Sci. Lett., 4 (2011) 1293-1301.
[48] E. Lilleodden, J. Zimmerman, S. Foiles, W. Nix, J. Mech. Phys. Solids, 51 (2003) 901-920.
[49] S.P. Timoshenko, J.M. Gere, Theory of elastic stability, McGraw-Hill, New York, 1961.
[50] L. Landau, E. Lifshitz, Theory of elasticity, Butterworth-Heinemann Oxford, 1986.
[51] A. Heidelberg, L.T. Ngo, B. Wu, M.A. Phillips, S. Sharma, T.I. Kamins, J.E. Sader, J.J. Boland, Nano Lett., 6 (2006) 1101-1106.
[52] H.S. Park, W. Cai, H.D. Espinosa, H. Huang, MRS Bull., 34 (2009) 178-183.
[53] W. Liang, M. Zhou, Proceedings of the Institution of Mechanical Engineers, Part C: Journal of Mechanical Engineering Science, 218 (2004) 599-606.
[54] R. Miller, V. Shenoy, Nanotechnology, 11 (2000) 139.
[55] H. Liang, M. Upmanyu, H. Huang, Phys. Rev. B, 71 (2005) 241403.

Figures and Tables

Table 1. Parameters of Morse potential for Cu-Cu atomic interaction. 1

Fig. 1. MD simulation model of a Cu NW under bending. The cylindrical rigid tip is placed right at the middle of the NW. 1

Fig. 2. *F-d* curve of Cu NW under the loading rate of 1 *m/s*. The NW size is 2.892 ×2.892 ×14.46 nm^3. 1

Fig. 3. *F-d* curves under different loading rates. (a) *F-d* curve during loading and unloading; (b) *F-d* curve at the beginning of loading; (c) *F-d* curve around the maximum displacement. 1

Fig. 4. Atomic configurations of Cu NWs: Loading rate of 50 *m/s*: (a1) & (a2) at the displacement of 1.1 nm, and (a3) when full unloaded; Loading rate of 15 *m/s*: (b1) & (b2) at the displacement of 1.05 nm, and (b3) when full unloaded; Loading rate of 1 *m/s*: (c1) & (c2) at the displacement of 1.05 nm, and (c3) when full unloaded. Figures in the first row are coloured according to the stress tensor value. The rest are coloured according to the *csp* value. 2

Fig. 5. *F-d* curves. (a) Unloading *F-d* curves under different loading rates; (b) *F-d* curves under different potentials. 2

Fig. 6. *F-d* curves for different loading paths. (a) Loading and unloading process with the maximum displacement of 1.3 *nm*; (b) Loading and unloading process with the maximum displacement of 2.9 *nm*; (c) Loading and unloading process with the maximum displacement of 4.5 *nm*; (d) Entire loading process together with fitting results from Eq. 5 and 6. 2

Fig. 7. Atomic configurations of Cu NW at different displacements. (a) *d*=2.9 *nm*; (b) *d*=2.9 *nm*, coloured according to the atomic stress tensor value; (c) Full unloaded after the maximum displacement of 2.9 *nm*; (d) *d*=4.5 *nm*; (e) *d*=7.7 *nm*. Figures a, c, d, e are coloured according to the *csp* value. 3

Fig. 8. MD results of Cu NWs with the length ranging from 14.46 *nm* to 32.535 *nm*. (a) *F-d* curves; (b) Comparison of estimated Young's modulus; (c) Comparison of estimated yield strength. 3

Tables:

Table 1. Parameters of Morse potential for Cu-Cu atomic interaction.

Parameters	D (eV)	a ($Å^{-1}$)	r_0 ($Å$)
M1	0.1	1.7	2.2
M2	0.087	5.14	2.05

Figures:

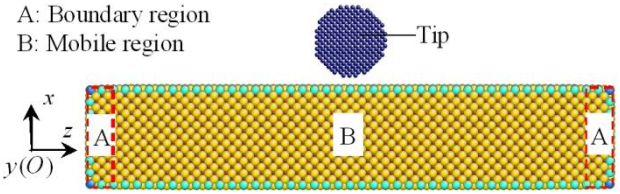

Fig. 1. MD simulation model of a Cu NW under bending. The cylindrical rigid tip is placed right at the middle of the NW.

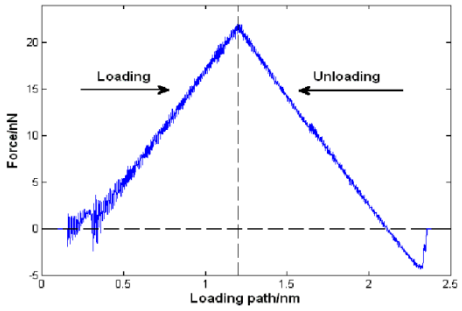

Fig. 2. *F-d* curve of Cu NW under the loading rate of 1 *m/s*. The NW size is 2.892×2.892×14.46 nm^3.

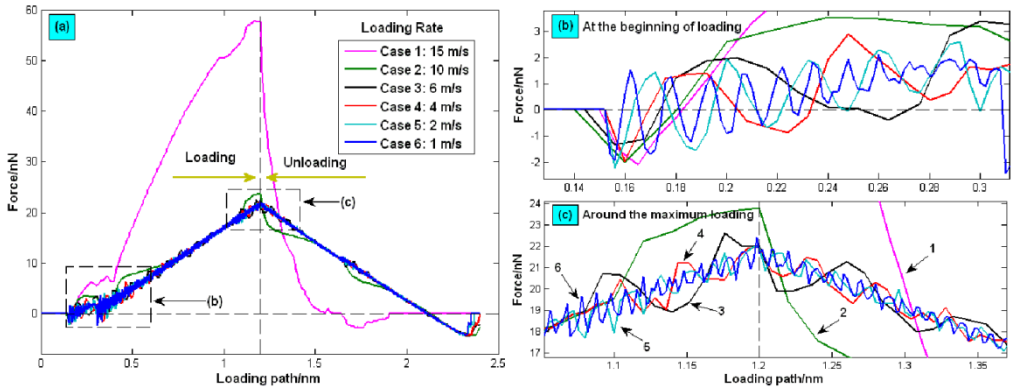

Fig. 3. *F-d* curves under different loading rates. (a) *F-d* curve during loading and unloading; (b) *F-d* curve at the beginning of loading; (c) *F-d* curve around the maximum displacement.

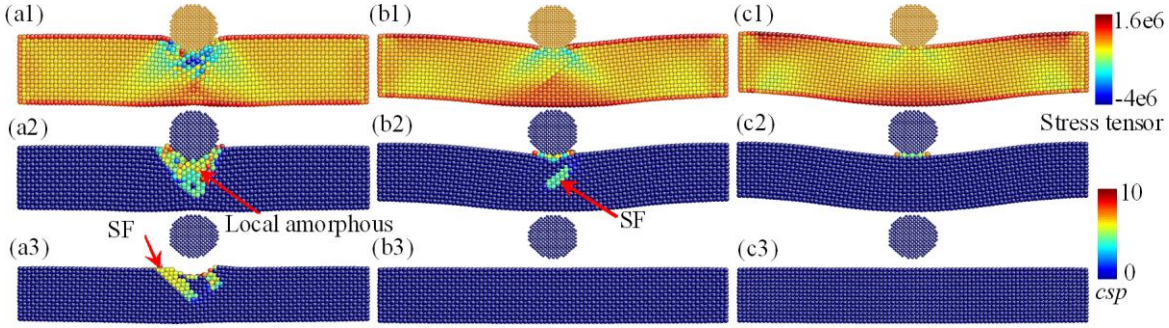

Fig. 4. Atomic configurations of Cu NWs: Loading rate of 50 *m/s*: (a1) & (a2) at the displacement of 1.1 nm, and (a3) when full unloaded; Loading rate of 15 *m/s*: (b1) & (b2) at the displacement of 1.05 nm, and (b3) when full unloaded; Loading rate of 1 *m/s*: (c1) & (c2) at the displacement of 1.05 nm, and (c3) when full unloaded. Figures in the first row are coloured according to the stress tensor value. The rest are coloured according to the *csp* value.

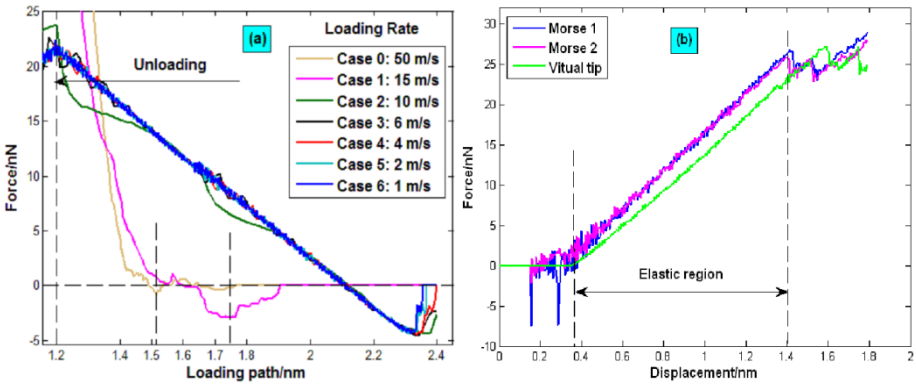

Fig. 5. *F-d* curves. (a) Unloading *F-d* curves under different loading rates; (b) *F-d* curves under different potentials.

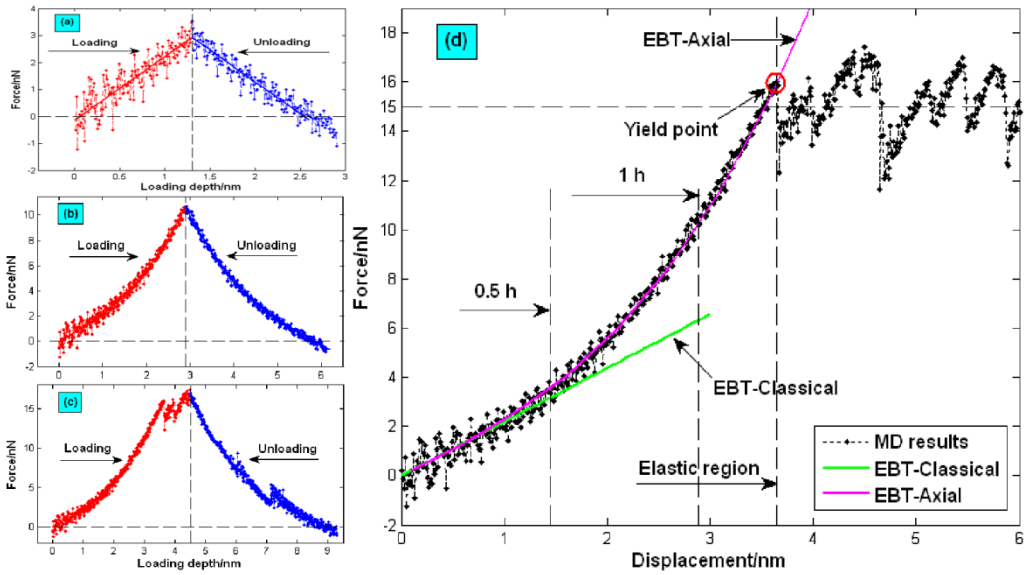

Fig. 6. *F-d* curves for different loading paths. (a) Loading and unloading process with the maximum displacement of 1.3 *nm*; (b) Loading and unloading process with the maximum displacement of 2.9 *nm*; (c) Loading and unloading process with the maximum displacement of 4.5 *nm*; (d) Entire loading process together with fitting results from Eq. 5 and 6.

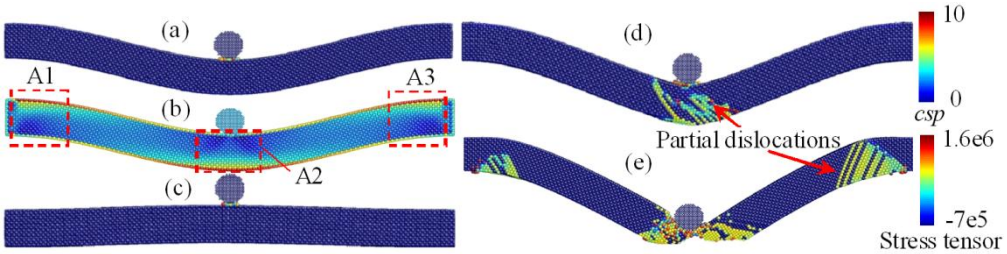

Fig. 7. Atomic configurations of Cu NW at different displacements. (a) *d*=2.9 *nm*; (b) *d*=2.9 *nm*, coloured according to the atomic stress tensor value; (c) Full unloaded after the maximum displacement of 2.9 *nm*; (d) *d*=4.5 *nm*; (e) *d*=7.7 *nm*. Figures a, c, d, e are coloured according to the *csp* value.

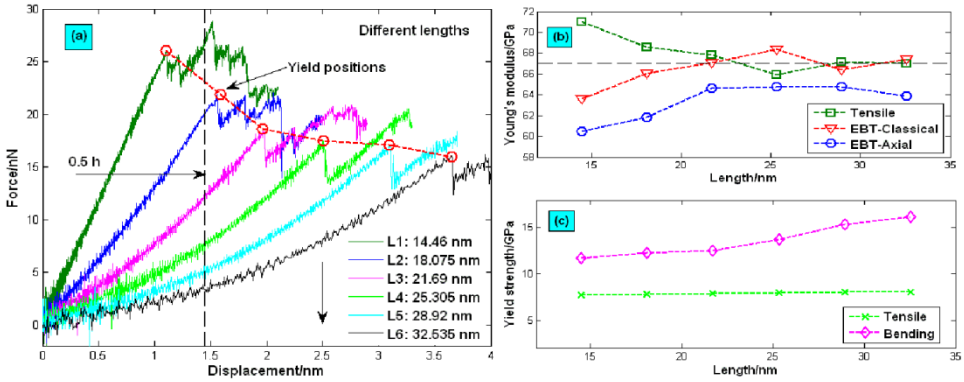

Fig. 8. MD results of Cu NWs with the length ranging from 14.46 *nm* to 32.535 *nm*. (a) *F-d* curves; (b) Comparison of estimated Young's modulus; (c) Comparison of estimated yield strength.